



Faculty Publications

---

2008-10-01

## Theory and Application of Motion Compensation for LFM-CW SAR

David G. Long  
david\_long@byu.edu

Evan C. Zaugg

Follow this and additional works at: <https://scholarsarchive.byu.edu/facpub>



Part of the [Electrical and Computer Engineering Commons](#)

### Original Publication Citation

Zaugg, E. C., and D. G. Long. "Theory and Application of Motion Compensation for LFM-CW SAR." *Geoscience and Remote Sensing, IEEE Transactions on* 46.1 (28): 299-8

---

### BYU ScholarsArchive Citation

Long, David G. and Zaugg, Evan C., "Theory and Application of Motion Compensation for LFM-CW SAR" (2008). *Faculty Publications*. 164.  
<https://scholarsarchive.byu.edu/facpub/164>

This Peer-Reviewed Article is brought to you for free and open access by BYU ScholarsArchive. It has been accepted for inclusion in Faculty Publications by an authorized administrator of BYU ScholarsArchive. For more information, please contact [ellen\\_amatangelo@byu.edu](mailto:ellen_amatangelo@byu.edu).

# Theory and Application of Motion Compensation for LFM-CW SAR

Evan C. Zaugg, *Student Member, IEEE*, and David G. Long, *Fellow, IEEE*

**Abstract**—Small low-cost high-resolution synthetic aperture radar (SAR) systems are made possible by using a linear frequency-modulated continuous-wave (LFM-CW) signal. SAR processing assumes that the sensor is moving in a straight line at a constant speed, but in actuality, an unmanned aerial vehicle (UAV) or airplane will often significantly deviate from this ideal. This nonideal motion can seriously degrade the SAR image quality. In a continuous-wave system, this motion happens during the radar pulse, which means that existing motion compensation techniques that approximate the position as constant over a pulse are limited for LFM-CW SAR. Small aircraft and UAVs are particularly susceptible to atmospheric turbulence, making the need for motion compensation even greater for SARs operating on these platforms. In this paper, the LFM-CW SAR signal model is presented, and processing algorithms are discussed. The effects of nonideal motion on the SAR signal are derived, and new methods for motion correction are developed, which correct for motion during the pulse. These new motion correction algorithms are verified with simulated data and with actual data collected using the Brigham Young University  $\mu$ SAR system.

**Index Terms**—Motion compensation, synthetic aperture radar (SAR).

## I. INTRODUCTION

VERY SMALL low-cost synthetic aperture radar (SAR) systems have recently been demonstrated as an alternative to the expensive and complex traditional systems [1]–[7]. The use of a frequency-modulated continuous-wave (FMCW) signal facilitates system miniaturization and low-power operation, which make it possible to fly these systems on small unmanned aerial vehicles (UAVs). The ease of operation and low operating costs make it possible to conduct extensive SAR studies without a large investment.

Recently, new processing methods have been developed to address issues specific to FMCW SAR [8]. The range-Doppler algorithm (RDA) [9] and the frequency (or chirp) scaling algorithm (FSA or CSA) [10] can be modified to compensate for the constant forward motion during the FMCW chirp. Non-linearities in the chirp can also be corrected [11], and squint-mode data can be processed [12]. In this paper, the problems caused by nonideal motion of a linear frequency-modulated continuous-wave (LFM-CW) SAR system are addressed, and new compensation algorithms are developed.

Manuscript received September 29, 2007; revised February 28, 2008. Current version published October 1, 2008.

The authors are with the Department of Electrical and Computer Engineering, Brigham Young University, Provo, UT 84602 USA.

Color versions of one or more of the figures in this paper are available online at <http://ieeexplore.ieee.org>.

Digital Object Identifier 10.1109/TGRS.2008.921958

Stripmap SAR processing assumes that the platform is moving in a straight line, at a constant speed, and with a consistent geometry with the target area. During data collection, whether in a manned aircraft or a UAV, there are deviations from this ideal as the platform changes its attitude and speed or is subjected to turbulence in the atmosphere. These displacements introduce variations in the phase history, the signal's time of flight to a target, and the sample spacing, all of which degrade the image quality. If the motion of the platform is known, then corrections can be made to the SAR data for more ideal image processing. Small aircraft and UAVs are more susceptible to atmospheric turbulence; thus, the need for motion compensation on these platforms is greater.

Motion compensation algorithms for traditional pulsed SAR have extensively been studied [13], [14], but the underlying differences with an LFM-CW signal make it a challenge to extend existing motion compensation methods to LFM-CW sensors. In pulsed SAR, the platform is assumed to be stationary during each pulse, and the motion takes place between pulses. With LFM-CW SAR, the signal is constantly being transmitted and received; thus, the motion takes place during the chirp.

This paper presents the development of new motion compensation algorithms that are suitable for use with both the RDA and the FSA (or CSA), which account for the motion during the chirp. The proposed algorithms also correct the range shift introduced by translational motion of magnitude greater than a single range bin without interpolation. First, in Section II, the theoretical underpinnings of LFM-CW SAR are developed, and processing methods are described. Section III shows the effects of nonideal motion. In Section IV, theoretical correction algorithms are developed and made practical by simplifying assumptions.

Section V presents simulation results in which a SAR system images a few point targets with nonideal motion. The known deviations are used to compensate for the effects of nonideal motion in the simulated data. A quantitative analysis of the simulation results is performed, which compares the proposed motion compensation algorithm to the traditional method. The new motion compensation scheme is applicable to a number of FMCW SAR systems, which are summarized in Section VI. The developed algorithm is applied to actual data from the Brigham Young University (BYU)  $\mu$ SAR data, and the results are presented. Motion data are provided by an inertial navigation system (INS) and GPS. The flight path data are interpolated between samples to provide position data for each sample of SAR data. The motion data are used to determine the necessary corrections that are introduced into the SAR data, effectively straightening the flight path.

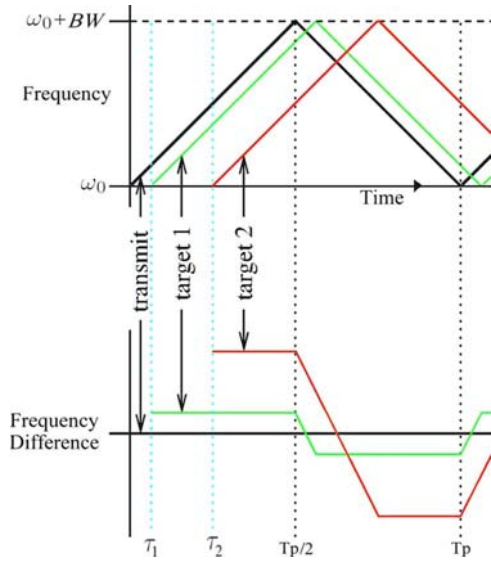


Fig. 1. (Top) Frequency change of a symmetric LFM-CW signal over time, together with the signal returns from two separate targets. (Bottom) Frequencies of the dechirped signal, with the times of flight  $\tau_1$  and  $\tau_2$ , due to the range determining the dechirped frequency. The relative sizes of  $\tau_1$ ,  $\tau_2$ , and  $T_p$  are exaggerated for illustrative purposes.

## II. LFM-CW SAR SIGNAL PROCESSING

In a symmetric LFM-CW chirp, the frequency of the signal increases from a starting frequency  $\omega_0$  and spans the bandwidth  $BW$ , at the chirp rate  $k_r = BW \cdot 2 \cdot \text{PRF}$ . The frequency then ramps back down, as shown in Fig. 1. This up-down cycle is repeated at the pulse repetition frequency (PRF), giving a pulse repetition interval of  $T_p$ . The transmitted up-chirp signal can be expressed in the time domain as

$$s_t(t, \eta) = e^{j(\phi + \omega_0 t + \pi k_r t^2)} \quad (1)$$

where  $t$  is the fast time,  $\eta$  is the slow time, and  $\phi$  is the initial phase. The down-chirp signal can be expressed similarly to the up-chirp signal, but with  $\omega_0 + BW$  as the starting frequency and  $-k_r$  as the chirp rate.

The received signal from a target at range  $R(t, \eta) = \sqrt{R_0^2 + v^2(t + \eta)^2}$ , with time delay  $\tau = 2R(t, \eta)/c$ , is

$$s_r(t, \eta) = e^{j(\phi + \omega_0(t - \tau) + \pi k_r(t - \tau)^2)} \quad (2)$$

where  $R_0$  is the range of closest approach of the target.

The transmit signal is mixed with the received signal and low-pass filtered in hardware, which is mathematically equivalent to multiplying (1) by the complex conjugate of (2). This results in the dechirped signal

$$s_{\text{dc}}(t, \eta) = e^{j(\omega_0 \tau + 2\pi k_r t \tau - \pi k_r \tau^2)}. \quad (3)$$

These raw data are then processed to create a SAR image.

Options for data processing include the RDA and the FSA (or CSA), as shown in Fig. 2. For RDA processing, this signal is range compressed with a fast Fourier transform (FFT) in the range direction and then taken to the range-Doppler domain with an FFT in the azimuth direction. Using standard interpolation methods, range cell migration (RCM) can be compensated,

but this is computationally costly. The Doppler shift introduced by the continuous forward motion of the platform can also be removed [9]. Azimuth compression is performed by multiplying by the azimuth-matched filter, i.e.,

$$H_{\text{az}}(f_\eta, R_0) = e^{j\frac{4\pi R_0}{\lambda} D(f_\eta, v)} \quad (4)$$

where  $D(f_\eta, v) = \sqrt{1 - \lambda^2 f_\eta^2 / 4v^2}$  is the range migration factor,  $v$  is the platform along-track velocity, and  $\lambda$  is the wavelength of the center transmit frequency.

Alternatively, the FSA (or CSA) [15] can also be modified to work with the dechirped data [16]. With the FSA, RCM can be compensated without interpolation. This advantage makes the FSA the preferred method for LFM-CW SAR processing. Fig. 3 compares the RDA (without RCM correction) and the FSA in processing data from the BYU  $\mu$ SAR.

FSA processing involves a series of Fourier transforms and phase multiplies. If a known nonlinearity exists in the FMCW chirp, it can be compensated by modifying the functions as in [10]. To start the FSA processing, an FFT is performed in the azimuth direction on the signal from (3). The resulting signal in the dechirped Doppler domain is

$$S(t, f_\eta) = e^{-j\frac{4\pi R_0 D(f_\eta, v)}{\lambda}} e^{-j\frac{4\pi k_r R_0 t}{c D(f_\eta, v)}} e^{j2\pi f_\eta t} e^{-j\pi k_r t^2}. \quad (5)$$

The frequency scaling function is applied with an additional term that removes the Doppler shift [10], i.e.,

$$H_1(t, f_\eta) = e^{-j(2\pi f_\eta t + \pi k_r t^2 (1 - D(f_\eta, v)))}. \quad (6)$$

A range FFT is performed, and the second function is applied, which corrects the residual video phase. Thus

$$H_2(f_r, f_\eta) = e^{(-j\pi f_r^2) / (k_r D(f_\eta, v))}. \quad (7)$$

An inverse FFT in the range direction is performed, followed by a function that performs inverse frequency scaling, i.e.,

$$H_3(t, f_\eta) = e^{-j\pi k_r t^2 [D(f_\eta, v)^2 - D(f_\eta, v)]}. \quad (8)$$

Here, the secondary range correction and bulk range shift phase function can be used, as in [16].

We again take the range FFT and apply the final filter that performs azimuth compression (4). An azimuth inverse FFT results in the final focused image.

## III. NONIDEAL MOTION ERRORS

The SAR processing algorithms described in Section II assume that the platform moves at a constant speed in a straight line. This is not the case in any actual data collection, as the platform experiences a variety of deviations from the ideal path. These deviations introduce errors in the collected data, which degrade the SAR image.

Translational motion causes platform displacement from the nominal ideal path. This results in the target scene changing in range during data collection. This range shift also causes inconsistencies in the target phase history. A target at range  $R$

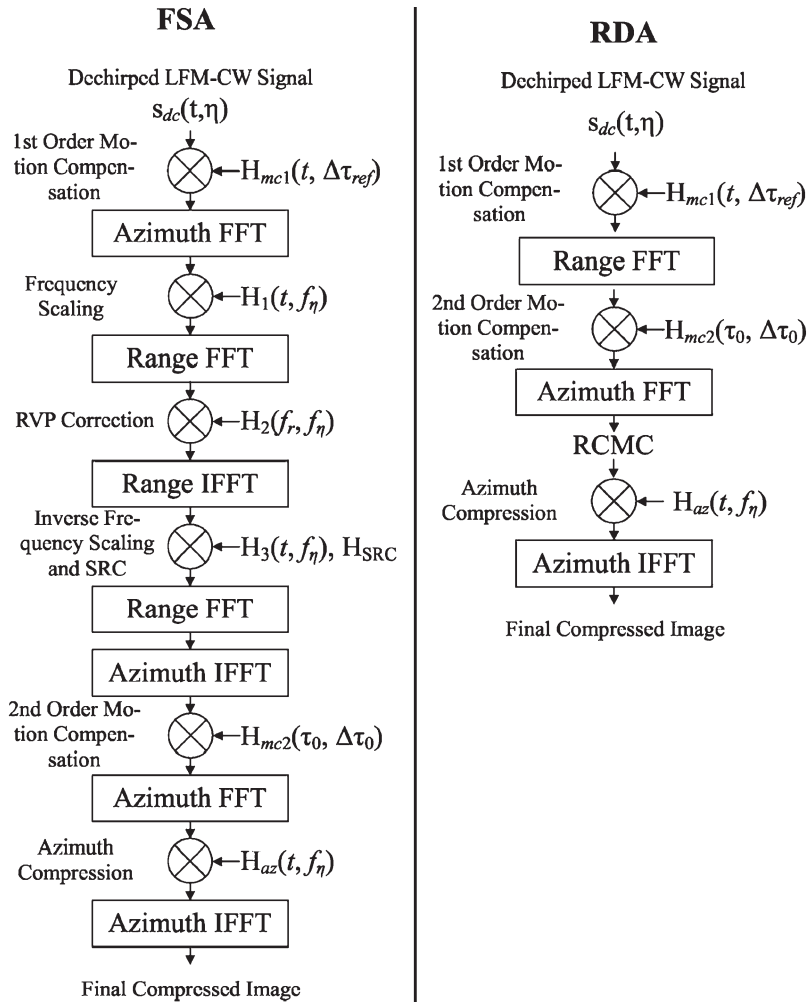


Fig. 2. Block diagram showing LFM-CW SAR processing using (left) the FSA and (right) RDA, including the proposed two-step motion compensation.

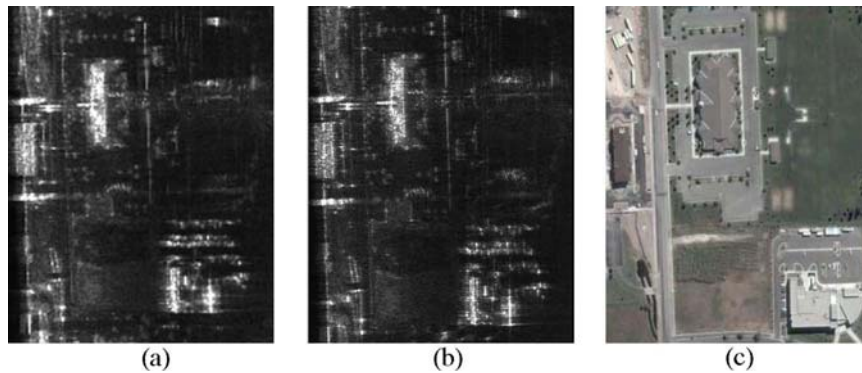


Fig. 3. Taken from a larger image, i.e., a 286 m  $\times$  360 m area of North Logan, UT. Imaged with the BYU  $\mu$ SAR operating at 5.62 GHz with a bandwidth of 80 MHz. The data were processed with the RDA and FSA. The horizontal axis is a slant range with the aircraft moving upward at image left. (a) Data processed with the RDA, without RCM correction. The entire collection was processed in 30.4 s. (b) Data processed with the FSA. The entire collection was processed in 84.3 s. (c) Aerial photograph for comparison purposes. It is clear that the focusing is better with the FSA and is worth the extraprocessing load.

is measured at range  $R + \Delta R$ , resulting in a frequency shift in the dechirped data. The dechirped signal in (3) then becomes

$$s_{\Delta dc}(t, \eta) = e^{j(\omega_0(\tau + \Delta\tau) + 2\pi k_r t(\tau + \Delta\tau) - \pi k_r(\tau + \Delta\tau)^2)} \quad (9)$$

where  $\Delta\tau = 2\Delta R/c$ . Targets that lie within the beamwidth that have a nonzero Doppler frequency experience a different change in range that is dependent on the azimuth position. This

is illustrated in Fig. 4, where the range to target  $A$  differently changes with motion than the range to target  $B$ .

Variations in along-track ground speed result in nonuniform spacing of the radar pulses on the ground. This nonuniform sampling of the Doppler spectrum results in erroneous calculations of the Doppler phase history.

Changes in pitch, roll, and yaw introduce errors of different kinds. The pitch displaces the antenna footprint on the ground,

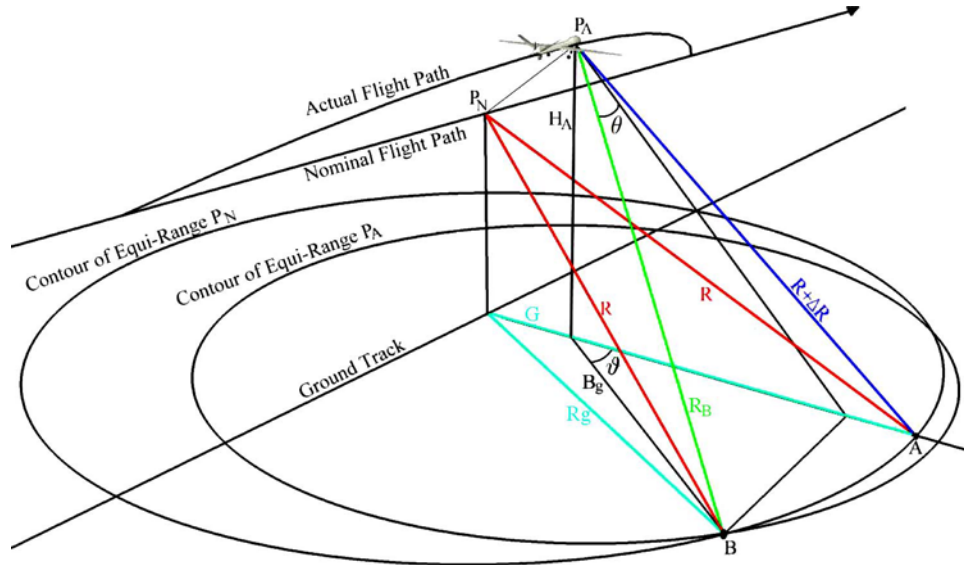


Fig. 4. SAR platform deviates from its nominal path, i.e., point  $P_N$ , resulting in a change in range to point  $A$  from  $R$  to  $R + \Delta R$ . Point  $B$  is nominally at a range  $R$ , but the deviation to point  $P_A$  changes the range to  $R_B$ , which is different from  $R + \Delta R$ .

the roll changes the antenna gain pattern over the target area, and the yaw introduces a squint. Pitch and yaw shift the Doppler centroid, with the shift being range dependent in the yaw case. If the Doppler spectrum is shifted so that a portion lies outside the Doppler bandwidth, then aliasing occurs. Azimuth compression produces ghost images at the azimuth locations where the Doppler frequency is aliased to zero.

#### IV. MOTION COMPENSATION

Previously developed methods of motion compensation are limited for correcting the nonideal motion of an LFM-CW SAR system. Methods like those of [17] apply bulk motion compensation to the raw data and a secondary correction to the range-compressed data. This works as an approximation for motion correction but relies on assuming that the platform is stationary during a pulse. In range compressing the data, we lose the ability to differentiate the motion over the chirp, which is problematic for LFM-CW SAR.

For an LFM-CW SAR signal, motion corrections can directly be applied to the raw dechirped data (9) or Doppler-dependent corrections are applied to the azimuth FFT of the raw data, in the dechirped Doppler domain. Because each data point contains information from every range, and the corrections are range and azimuth dependent, any corrections applied in the dechirped Doppler domain are only valid for a single range and a single azimuth value. However, with approximations, these restrictions can be relaxed.

##### A. Theoretical Treatment

In general, motion data are collected at a much slower rate than SAR data. For LFM-CW SAR, motion data must be interpolated so that every sample of SAR data has corresponding position information (as opposed to only each pulse having position data). Each data point also needs to have a corresponding location on the ideal path to which the error is corrected. For a target at range  $R$ ,  $\Delta R$  is calculated from the

difference between the distance to the ideal track and the actual track. The flat-terrain geometry of Fig. 4 is assumed. If more precise knowledge of the terrain is available, then the model can be adjusted [18], [19]. Knowing the coordinates of target  $A$ , the actual flight path (point  $P_A$ ), and the nominal flight path (point  $P_N$ ), the distances  $R$  and  $R + \Delta R$  can be calculated from the geometry. Again,  $\Delta \tau = 2\Delta R/c$ , but  $\Delta \tau$  is updated for every data sample. The motion errors are corrected using our correction filter

$$H_{MC}(t, \Delta \tau) = e^{-j(\omega_0 \Delta \tau + 2\pi k_r t \Delta \tau - \pi k_r (2\tau \Delta \tau - \Delta \tau^2))}. \quad (10)$$

When applied to the data (in the raw dechirped time domain or the dechirped Doppler domain), this shifts the range of the target and adjusts the phase.

There are targets in the beamwidth at the same range but different azimuth positions that experience a different range shift due to translational motion. For a given azimuth position, as shown in Fig. 4, target  $B$  is at a position where it has the Doppler frequency  $f_\eta$ . The angle to target  $B$  is

$$\theta(f_\eta) = \sin^{-1} \left( \frac{f_\eta \lambda}{2v} \right). \quad (11)$$

Working through some particularly unpleasant geometry (see Appendix B), the angle on the ground (as defined in Fig. 4), i.e.,  $\vartheta(\theta(f_\eta), R_g, G, H_A)$ , is found. From  $\vartheta$ , we find the ground range, i.e.,

$$B_g(f_\eta) = -\cos(\vartheta)G \pm \sqrt{\cos^2(\vartheta)G^2 + R_g^2 - G^2} \quad (12)$$

and the actual range to target  $B$ , i.e.,

$$R_B(f_\eta) = \sqrt{H_A^2 + B_g^2}. \quad (13)$$

We then find  $\Delta R = R - R_B(f_\eta)$  and  $\Delta \tau = 2\Delta R(f_\eta)/c$  and apply (10) in the dechirped Doppler domain. This correction is valid for a single range and a single azimuth position.



Exactly correcting the motion errors in this way is computationally taxing. For every pixel of the final image, the correction is applied in the dechirped Doppler domain for the given range and azimuth position. The data are processed through range compression, and a single data point is kept. A composite range-compressed image is created from these individual points, and the final image is formed through azimuth compression. Fortunately, there are approximations that can be made to reduce the computational load while still maintaining the advantages of this method.

### B. Simplifying Approximations

If the beamwidth is narrow, then the errors due to motion can be assumed to be constant for a given range across the Doppler bandwidth. This is called center-beam approximation [20] and is used in many motion compensation algorithms. The errors induced by this approximation are detailed in [21]. A number of methods have been proposed as alternatives to this approximation, as discussed in [22]. When using this approximation, we apply the correction filter (10) to the raw data. The correction is valid for only a single range; thus, a composite range-compressed image is created and then azimuth compressed to form the final image.

Further simplification is possible by splitting the correction into two steps. The first step applies the correction for a reference range  $R_{\text{ref}}$ .  $\Delta R_{\text{ref}}$  is calculated as before with  $\Delta\tau_{\text{ref}} = 2\Delta R_{\text{ref}}/c$  and  $\tau_{\text{ref}} = 2R_{\text{ref}}/c$ . Then, the correction is

$$H_{\text{MC1}}(t, \Delta\tau_{\text{ref}}) = \exp(-j(\omega_0\Delta\tau_{\text{ref}} + 2\pi k_r t \Delta\tau_{\text{ref}} - \pi k_r (2\tau_{\text{ref}}\Delta\tau_{\text{ref}} - \Delta\tau_{\text{ref}}^2))). \quad (14)$$

The second step applies differential correction after range compression. For this step, position information is averaged over each pulse. This is due to the fact that when LFM-CW data are range compressed, each range bin is formed from data that span the entire pulse. This second-order correction is calculated for each range bin  $R_0$  with a calculated  $\Delta R_0$ ,  $\Delta\tau_0 = 2\Delta R_0/c$ , and  $\tau_0 = 2R_0/c$ . It is simply  $H_{\text{MC}}(t, \Delta\tau_0)/H_{\text{MC}}(t, \Delta\tau_{\text{ref}})$  or

$$H_{\text{MC2}}(\tau_0, \Delta\tau_0) = \exp(j(-\omega_0\Delta\tau_0 + 2\pi k_r \tau_0 \Delta\tau_0 - \pi k_r \Delta\tau_0^2 + \omega_0\Delta\tau_{\text{ref}} - 2\pi k_r \tau_{\text{ref}} \Delta\tau_{\text{ref}} + \pi k_r \Delta\tau_{\text{ref}}^2)). \quad (15)$$

This is similar to the traditional motion compensation model but with a couple of advantages. The motion during the pulse is still considered in applying the initial correction, thus making it suitable for LFM-CW SAR. In addition, the range shift caused by translational motion is corrected without interpolation. Fig. 5 shows the simulated point targets focused by correcting the nonideal motion using this method.

The errors introduced by this two-step approximate method are much less than the errors from the traditional method. We denote the phase error caused by approximations in the motion correction function as

$$\phi_E = \frac{4\pi\Delta R_e}{\lambda} \quad (16)$$

where  $\Delta R_e$  is the error in the calculation of the required correction due to translational motion. For the proposed correction,

TABLE I  
SIMULATION PARAMETERS

Chirp Bandwidth (MHz)	250
Center Frequency (GHz)	5.62
Azimuth Beamwidth	12°
Pulse Repetition Frequency (Hz)	320
Sample Rate (Hz)	327680

TABLE II  
THEORETICAL VALUES

Range Resolution (meters)	0.5996
Azimuth Resolution (meters)	0.1274

there is no error caused by the motion during the chirp, whereas for traditional motion compensation, the first-order correction has the error

$$\Delta R_{e1} = \Delta R_{\text{ref}}(t) - \Delta R'_{\text{ref}} \quad (17)$$

where  $\Delta R_{\text{ref}}(t)$  is the time-varying translational motion correction that takes into account the motion during the chirp, and  $\Delta R'_{\text{ref}}$  is constant for each pulse. For a SAR with the parameters listed in Tables I and II, with a velocity of 25 m/s and translational motion of 0.5 m over 10 m of along-track distance, the maximum phase error is calculated to be 0.4598 rad.

For the second-order motion compensation, the error is the same for both the proposed motion compensation scheme and the traditional method. It is calculated as

$$\Delta R_{e2} = (\Delta R_{\text{ref}}(t) - \Delta R_0(t)) - (\Delta R'_{\text{ref}} - \Delta R'_0) \quad (18)$$

where  $\Delta R'_{\text{ref}}$  and  $\Delta R'_0$  are constant over the chirp. As an example, using the same 0.5-m translational error with a platform height of 100 m, a reference range of 141.4 m, and a target range of 111.8 m, the maximum second-order phase error is calculated to be 0.0238 rad, which is the total error of the proposed method. Thus, it is shown that the proposed method has a phase error that is an order of magnitude less than traditional motion compensation.

## V. MOTION COMPENSATION OF SIMULATED DATA

Fig. 5 and Table III show the results of an analysis of simulated LFM-CW SAR data. An array of point targets is used for the qualitative analysis, and a single point target is used for the quantitative analysis. The proposed motion compensation algorithm is compared to traditional motion compensation in the presence of severe translation motion and to an ideal collection made with ideal motion. The proposed motion compensation results are very near the ideal and much better than those of the traditional method. Of note are the measured improvements in range resolution (51%) and azimuth resolution (15%). The theoretical azimuth resolution is not reached, even with ideal motion, because of the defocusing due to the change in wavelength over the chirp.

## VI. FMCW SAR SYSTEMS

The proposed motion compensation scheme is suitable for a number of recently developed FMCW SAR systems. The

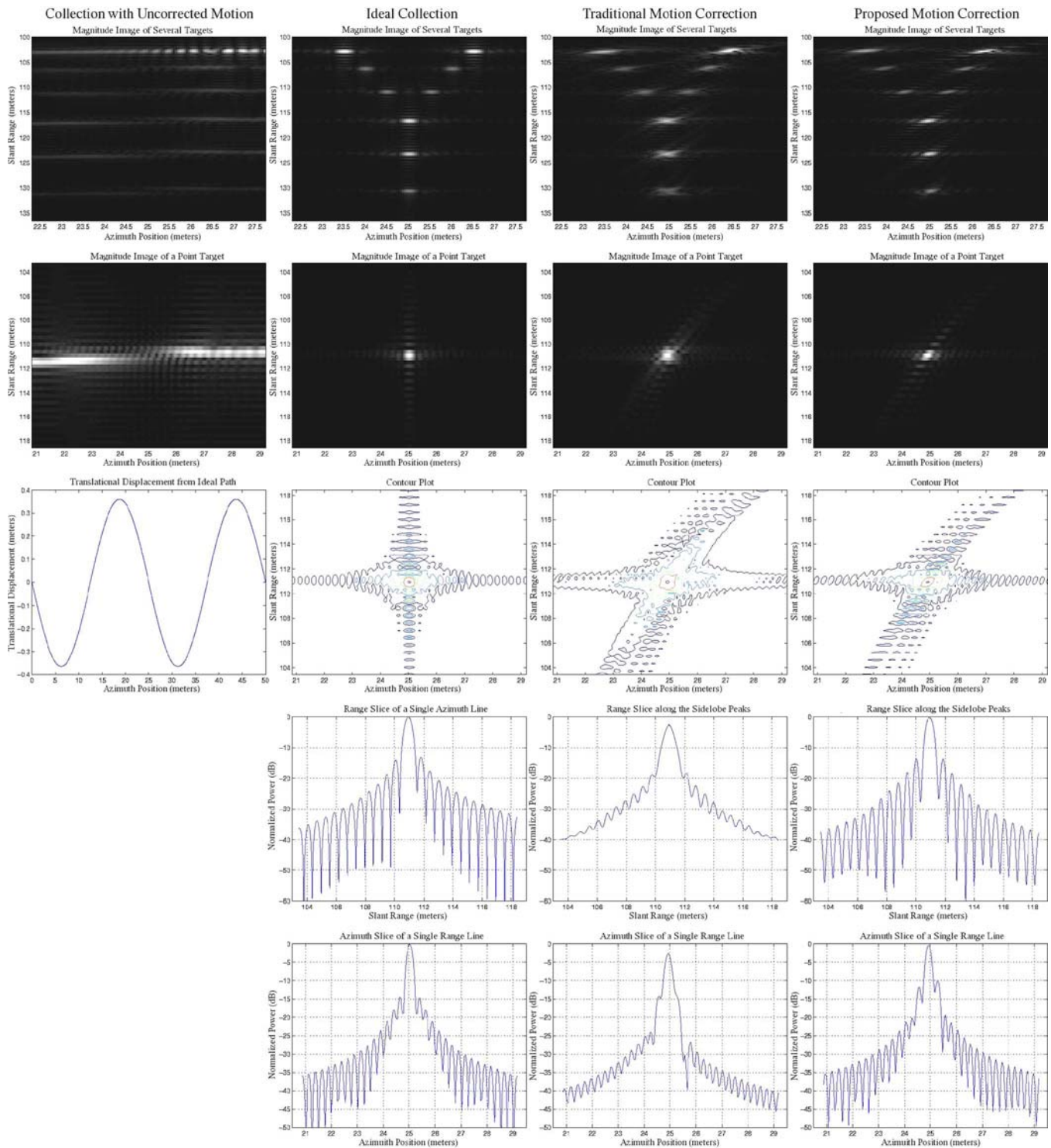


Fig. 5. Simulated LFM-CW SAR data of an array of point targets and a single point target. The first column shows the motion errors, whereas the second column shows an ideal collection without any motion errors. The third column shows motion correction using the traditional compensation method, whereas the fourth column shows the proposed motion compensation method. The power is normalized to the peak of the ideal collection. In this example, the nonideal motion is sinusoidal. The principal component of the translational motion while the target is in the main beamwidth is moving toward the target. This results in the corrected targets appearing “squinced.”

BYU  $\mu$ SARs are small, student-built, low-power, LFM-CW SAR systems [1]. They weigh less than 2 kg, including antennas and cabling, and consume 18 W of power. The  $\mu$ SAR systems operate at C- or L-band with bandwidths of 80–160 MHz. Units have successfully been flown in manned aircraft and on UAVs. Imaged areas include the arctic and areas in Utah and Idaho.

The BYU  $\mu$ SAR is flown with an MMQ-G INS/GPS unit from Systron Donner Inertial, which measures the motion of the aircraft. SAR and motion data are collected together and stored onboard or downlinked to a ground station. As discussed, the motion data are interpolated and matched with the actual SAR data. The results are shown in Fig. 6, where the data collected

TABLE III  
MEASURED SIMULATION VALUES

	Ideal Collection	Traditional Correction	Proposed Correction
<b>Range</b>			
Resolution (m)	0.647	0.919	0.6048
PSLR (dB)	13.37	18.49	13.77
ISLR (dB)	10.69	12.79	10.83
<b>Azimuth</b>			
Resolution (m)	0.313	0.358	0.309
PSLR (dB)	14.49	11.93	9.70
ISLR (dB)	10.62	12.57	7.99
Processing Time (s)	7.525	10.691	10.677

from a UAV show that the motion corrections improve the focusing of an array of corner reflector targets. A more detailed description of the  $\mu$ SAR system is found in Appendix A. A number of other small FMCW SARs are described in the following.

The MISAR [2] developed by EADS was designed to fly on small UAVs having a weight of less than 4 kg and power consumption under 100 W. The system operates at Ka-band (35 GHz) and produces images with  $0.5 \text{ m} \times 0.5 \text{ m}$  resolution. SAR and motion data (from an onboard INS) are transmitted to the ground via a 5-MHz analog video link. The nonideal motion is compensated using the INS data and autofocus.

The Delft University of Technology has developed a demonstrator system [3] with a center frequency of 10 GHz and a variable bandwidth of 130–520 MHz. Algorithms have been developed that compensate for nonlinearities in the chirp [11] and the continuous forward motion during the chirp [23]. An INS unit is used to measure the aircraft motion.

The MINISARA [4] from the Universidad Politécnic de Madrid is a portable SAR system with a center frequency of 34 GHz and a bandwidth of 2 GHz. The system is small ( $24 \times 16 \times 9 \text{ cm}$ ) and lightweight (2.5 kg). The motion compensation relies on autofocus algorithms.

The ImSAR NanoSAR [5] is a 1-lb SAR that is specifically built for use on small UAVs.

The DRIVE from ONERA [6] has a central frequency of 35 GHz and a bandwidth of about 800 MHz. The goal is to develop a 3-D SAR imaging system, and studies include compensating for the motion of the wings that carry the antennas.

The FGAN ARTINO [7] is a 3-D imaging radar similar to the ONERA project that operates at Ka-band. A custom INS was developed for the project and is used for motion compensation and UAV control.

## VII. CONCLUSION

In this paper, the effects of nonideal motion on an LFM-CW SAR signal have been explored, and corrective algorithms have been developed. Motion compensation has successfully been applied to simulated and real SAR data by taking into account the motion during the pulse and correcting the motion-induced range shift without interpolation. The small size of LFM-CW SAR, like the BYU  $\mu$ SAR, makes it possible for LFM-

CW SAR to operate from a small aircraft or UAV, which is particularly susceptible to the effects of atmospheric turbulence. With motion measurements, the negative effects of nonideal motion can be corrected, extending the utility of small LFM-CW SAR.

## APPENDIX A BYU $\mu$ SAR SYSTEM DESCRIPTION

The BYU  $\mu$ SAR meets the low power and cost requirements for flight on a UAV by employing an LFM-CW signal that maximizes the pulse length, allowing LFM-CW SAR to maintain a high signal-to-noise ratio while transmitting with less peak power than pulsed SAR [24]. While continuously transmitting, the frequency of the transmit signal repeatedly increases and decreases at the PRF.

The  $\mu$ SAR dechirps the received signal by mixing it with the transmitted signal. This simplifies the sampling hardware by lowering the required sampling frequency, although a higher dynamic range is needed.

A simplified block diagram of the  $\mu$ SAR design is shown in Fig. 7. The BYU  $\mu$ SAR system is designed to minimize size and weight using a stack of custom microstrip circuit boards without any enclosure. The system measures  $3 \text{ in} \times 3.4 \text{ in} \times 4 \text{ in}$  and weighs less than 2 kg, including antennas and cabling. Component costs of a few thousand dollars are kept low by using off-the-shelf components as much as possible (Fig. 8).

The UAV supplies the  $\mu$ SAR with either +18 Vdc or +12 Vdc. The power subsystem uses standard dc/dc converters to supply the various voltages needed in the system. Power consumption during operation is nominally 18 W, with slightly more required for initial start-up. The  $\mu$ SAR is designed for “turn-on and forget” operation. Once powered up, the system continuously collects data for up to an hour. The data are stored onboard for postflight analysis.

The core of the system is a 100-MHz STALO. From this single source, the frequencies for operating the system are derived, including the sample clock and the radar chirp. The LFM-CW transmit chirp is digitally created using a direct digital synthesizer (DDS), which is controlled by a programmable IC microcontroller. Switches control the PRF settings, allowing it to be varied (128–2886 Hz) for flying at different heights and speeds. The programmable DDS also generates the sample clock coherent with the LFM signal.

The  $\mu$ SAR signal is transmitted with a power of 28 dBmW at a center frequency of 5.56 or 1.72 GHz and a bandwidth of 80–160 MHz. The range resolution of an LFM chirp is inversely proportional to the bandwidth of the chirp; thus, the  $\mu$ SAR has a range resolution of 1.875 m at 80 MHz and 0.9375 m at 160 MHz.

At C-band, two identical custom microstrip antennas, each consisting of a  $2 \times 8$  patch array, are used in a bistatic configuration. The antennas are constructed from coplanar printed circuit boards sandwiched together, a symmetric feed structure on the back of one board and the patch array on the front of another, with pins feeding the signal through the boards. The antennas are approximately  $4 \text{ in} \times 12 \text{ in}$  and have an azimuth 3-dB beamwidth of  $8.8^\circ$  and an elevation 3-dB beamwidth of



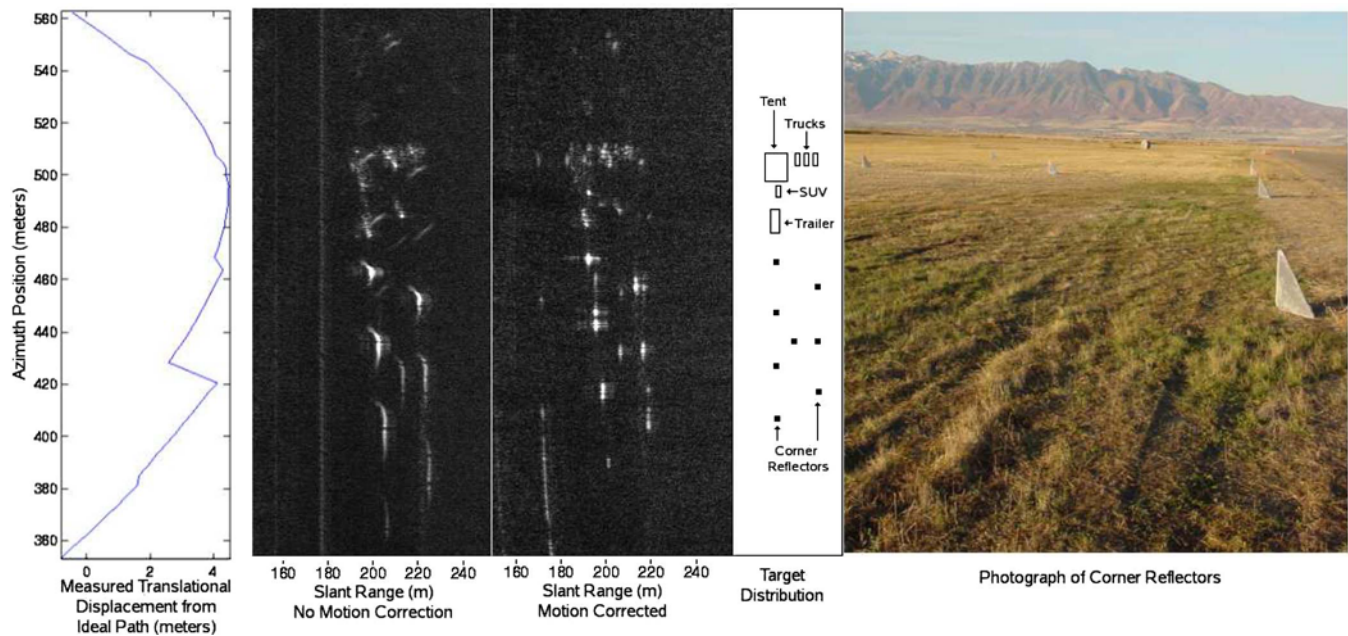


Fig. 6. Area of the airport at Logan, UT, imaged with a 160-MHz bandwidth C-band  $\mu$ SAR flown on a UAV and processed with the FSA, with corner reflector targets arrayed in a field. From left to right: The translational motion errors calculated from the INS motion data, the processed image without motion compensation, the image after applying the proposed compensation scheme, the arrangement of targets in the image, and a photograph taken near the trailer. The limitations of the INS motion sensor are noticeable in the inconsistency of the measured translational displacement, which results in the defocusing of a few of the targets in the compensated image.

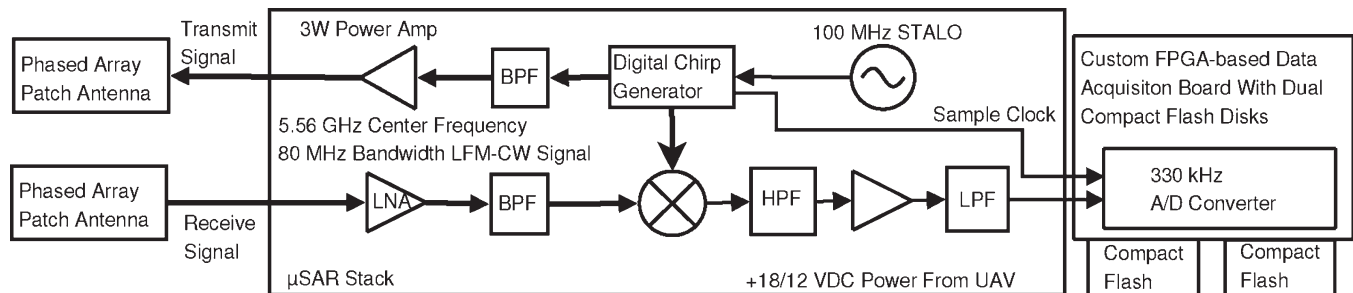


Fig. 7. Simplified BYU  $\mu$ SAR block diagram.

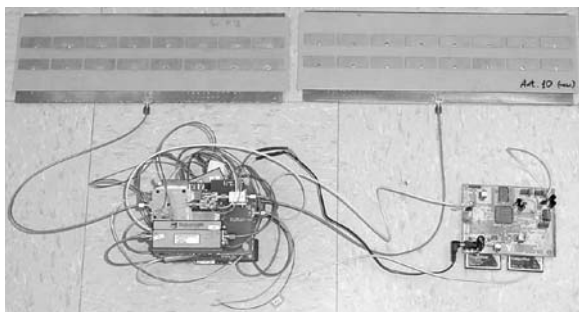


Fig. 8. Photograph of a complete BYU  $\mu$ SAR system ready for flight on a small UAV.

$50^\circ$ . The azimuth resolution is approximately equal to half the antenna length (0.15 m) in azimuth. Multilook averaging is used for creating images with the azimuth resolution equal to the range resolution. The L-band system uses antennas consisting of a  $2 \times 4$  array of fat dipoles.

The return signal is amplified and mixed with the transmit signal. This dechirped signal is filtered and then sampled with

a 16-bit analog-to-digital converter at 328.947 kHz. A custom field-programmable gate array board was designed to sample the signal and store the data on a pair of 1-GB Compact Flash disks. The data are continuously collected at a rate of 0.63 MB/s and either stored onboard or transmitted to a ground station.

Data processing for the BYU  $\mu$ SAR [25] follows the procedures outlined in the main body of this paper.

The Systron Donner Inertial MMQ-G INS/GPS unit is used with the BYU  $\mu$ SAR because of its small size ( $9.4 \text{ in}^3$ ) and weight ( $< 0.5 \text{ lb}$ ). It provides position and attitude solutions at a rate of 10 Hz. The solution messages are transmitted to the  $\mu$ SAR using RS-232 and stored with the SAR data.

## APPENDIX B NONZERO DOPPLER GEOMETRY CALCULATIONS

As defined in Fig. 4, the range  $R + \Delta R$  and the angle  $\theta$  are derived from the SAR data, and the height  $H_A$  and the range  $R$  are found from the motion data. We define a right triangle on the ground with hypotenuse  $B_g$  and sides  $B_g \cdot \cos(\vartheta)$  and

$B_g \cdot \sin(\vartheta)$ . We take the angle  $\phi$  to be between the lines  $R_g$  and  $G$ . From this, we get the following equalities:

$$\sin(\phi) = \frac{B_g \cdot \sin(\vartheta)}{R_g} \quad (19)$$

$$\cos(\phi) = \frac{G + B_g \cdot \cos(\vartheta)}{R_g} \quad (20)$$

$$\arcsin\left(\frac{B_g \cdot \sin(\vartheta)}{R_g}\right) = \arccos\left(\frac{G + B_g \cdot \cos(\vartheta)}{R_g}\right). \quad (21)$$

This gives us two unknowns, namely,  $B_g$  and  $\vartheta$ . Then, we introduce another equation, i.e.,

$$\tan(\theta) = \frac{B_g \cdot \sin(\vartheta)}{\sqrt{(B_g \cdot \cos(\vartheta))^2 + H_A^2}}. \quad (22)$$

Equations (21) and (22) are simultaneously solved for  $\vartheta$  and  $B_g$ . The closed-form solution can easily be found using a symbolic solver. Unfortunately, the resulting equation is too large to be printed here. However, tedious the solution may be, given the input values, a computer has no difficulty in producing the correct result.

## REFERENCES

- [1] E. C. Zaugg, D. L. Hudson, and D. G. Long, "The BYU  $\mu$ SAR: A small, student-built SAR for UAV operation," in *Proc. Int. Geosci. Remote Sens. Symp.*, Denver, CO, Aug. 2006, pp. 411–414.
- [2] M. Edrich, "Design overview and flight test results of the miniaturised SAR sensor MISAR," in *Proc. 1st EURAD*, Amsterdam, The Netherlands, Oct. 2004, pp. 205–208.
- [3] A. Meta, J. J. M. de Wit, and P. Hoogeboom, "Development of a high resolution airborne millimeter wave FM-CW SAR," in *Proc. 1st EURAD*, Amsterdam, The Netherlands, Oct. 2004, pp. 209–212.
- [4] P. Almorox-Gonzalez, J. T. Gonzalez-Partida, M. Burgos-Garcia, B. P. Dorta-Naranjo, C. de la Morena-Alvarez-Palencia, and L. Arche-Andradas, "Portable high resolution LFM-CW radar sensor in millimeter-wave band," in *Proc. SENSORCOMM*, Valencia, Spain, Oct. 2007, pp. 5–9.
- [5] L. Harris, "ImSAR and in situ introduce the one-pound nanoSAR(TM), miniature synthetic aperture radar," *ImSAR Micro Miniature Synthetic Aperture Radar*, Aug. 29, 2006. [Online]. Available: <http://www.imsar.net>
- [6] J. Nouvel, H. Jeuland, G. Bonin, S. Roques, O. Du Plessis, and J. Peyret, "A Ka band imaging radar: DRIVE on board ONERA motor-glider," in *Proc. Int. Geosci. Remote Sens. Symp.*, Denver, CO, Aug. 2006, pp. 134–136.
- [7] M. Weib and J. H. G. Ender, "A 3D imaging radar for small unmanned airplanes—ARTINO," in *Proc. EURAD*, Paris, France, Oct. 2005, pp. 209–212.
- [8] A. Meta, P. Hoogeboom, and L. P. Ligthart, "Signal processing for FMCW SAR," *IEEE Trans. Geosci. Remote Sens.*, vol. 45, no. 11, pp. 3519–3532, Nov. 2007.
- [9] J. J. M. de Wit, A. Meta, and P. Hoogeboom, "Modified range-Doppler processing for FM-CW synthetic aperture radar," *IEEE Geosci. Remote Sens. Lett.*, vol. 3, no. 1, pp. 83–87, Jan. 2006.
- [10] A. Meta, P. Hoogeboom, and L. P. Ligthart, "Non-linear frequency scaling algorithm for FMCW SAR data," in *Proc. 3rd Eur. Radar Conf.*, Sep. 2006, pp. 9–12.
- [11] A. Meta, P. Hoogeboom, and L. P. Ligthart, "Range non-linearities correction in FMCW SAR," in *Proc. Int. Geosci. Remote Sens. Symp.*, Denver, CO, Aug. 2006, pp. 403–406.
- [12] Z. H. Jiang, K. Huangfu, and J. W. Wan, "A chirp transform algorithm for processing squint mode FMCW SAR data," *IEEE Geosci. Remote Sens. Lett.*, vol. 4, no. 3, pp. 377–381, Jul. 2007.
- [13] J. C. Kirk, "Motion compensation for synthetic aperture radar," *IEEE Trans. Aerosp. Electron. Syst.*, vol. AES-11, no. 3, pp. 338–348, May 1975.
- [14] D. R. Stevens, I. G. Cumming, and A. L. Gray, "Options for airborne interferometric SAR motion compensation," *IEEE Trans. Geosci. Remote Sens.*, vol. 33, no. 2, pp. 409–420, Mar. 1995.
- [15] I. G. Cumming and F. H. Wong, *Digital Processing of Synthetic Aperture Radar Data*. Norwood, MA: Artech House, 2005.
- [16] J. Mittermayer, A. Moreira, and O. Loffeld, "Spotlight SAR data processing using the frequency scaling algorithm," *IEEE Trans. Geosci. Remote Sens.*, vol. 37, no. 5, pp. 2198–2214, Sep. 1999.
- [17] A. Moreira and Y. Huang, "Airborne SAR processing of highly squinted data using a chirp scaling approach with integrated motion compensation," *IEEE Trans. Geosci. Remote Sens.*, vol. 32, no. 5, pp. 1029–1040, Sep. 1994.
- [18] K. A. C. de Macedo and R. Scheiber, "Precise topography- and aperture-dependent motion compensation for airborne SAR," *IEEE Trans. Geosci. Remote Sens.*, vol. 2, no. 2, pp. 172–176, Apr. 2005.
- [19] P. Prats, A. Reigber, and J. J. Mallorqui, "Topography-dependent motion compensation for repeat-pass interferometric SAR systems," *IEEE Trans. Geosci. Remote Sens.*, vol. 2, no. 2, pp. 206–210, Apr. 2005.
- [20] G. Fornaro, "Trajectory deviations in airborne SAR: Analysis and compensation," *IEEE Trans. Aerosp. Electron. Syst.*, vol. 35, no. 3, pp. 997–1009, Jul. 1999.
- [21] G. Fornaro, G. Franceschetti, and S. Perna, "On center-beam approximation in SAR motion compensation," *IEEE Trans. Geosci. Remote Sens.*, vol. 3, no. 2, pp. 276–280, Apr. 2006.
- [22] P. Prats, K. A. Camara de Macedo, A. Reigber, R. Scheiber, and J. J. Mallorqui, "Comparison of topography- and aperture-dependent motion compensation algorithms for airborne SAR," *IEEE Geosci. Remote Sens. Lett.*, vol. 4, no. 3, pp. 349–353, Jul. 2007.
- [23] A. Meta, P. Hoogeboom, and L. P. Ligthart, "Correction of the effects induced by the continuous motion in airborne FMCW SAR," in *Proc. IEEE Conf. Radar*, Apr. 2006, pp. 358–365.
- [24] F. T. Ulaby, R. K. Moore, and A. K. Fung, *Microwave Remote Sensing Active and Passive*, vol. 1. Norwood, MA: Artech House, 1981.
- [25] M. I. Duersch, "BYU micro-SAR: A very small, low-power, LFM-CW synthetic aperture radar," M.S. thesis, Brigham Young Univ., Provo, UT, 2004.



**Evan C. Zaugg** (S'06) received the B.S. degree in electrical engineering in 2005 from Brigham Young University (BYU), Provo, UT, where he is currently working toward the Ph.D. degree.

He has been with the Microwave Remote Sensing Laboratory, BYU, since 2004. His research interest includes synthetic aperture radar system design, hardware, and signal processing.



**David G. Long** (S'80–M'82–SM'98–F'07) received the Ph.D. degree in electrical engineering from the University of Southern California, Los Angeles, in 1989.

From 1983 to 1990, he was with the Jet Propulsion Laboratory (JPL), National Aeronautics and Space Administration (NASA), where he developed advanced radar remote sensing systems. While at JPL he was the Project Engineer on the NASA Scatterometer (NSCAT) project, which flew from 1996 to 1997. He also managed the SCANSAR project, the precursor to SeaWinds, which was launched in 1999 and 2002. He is currently a Professor with the Department of Electrical and Computer Engineering, Brigham Young University, Provo, UT, where he teaches upper-division and graduate courses in communications, microwave remote sensing, radar, and signal processing, and is the Director of the BYU Center for Remote Sensing. He is the Principal Investigator on several NASA-sponsored research projects in remote sensing. He is the author or coauthor of more than 275 publications in signal processing and radar scatterometry. His research interests include microwave remote sensing, radar theory, space-based sensing, estimation theory, signal processing, and mesoscale atmospheric dynamics.

Dr. Long is an Associate Editor of the IEEE GEOSCIENCE AND REMOTE SENSING LETTERS. He has received the NASA Certificate of Recognition several times.